

This work was written as part of one of the author's official duties as an Employee of the United States Government and is therefore a work of the United States Government. In accordance with 17 U.S.C. 105, no copyright protection is available for such works under U.S. Law.

Public Domain Mark 1.0

<https://creativecommons.org/publicdomain/mark/1.0/>

Access to this work was provided by the University of Maryland, Baltimore County (UMBC) ScholarWorks@UMBC digital repository on the Maryland Shared Open Access (MD-SOAR) platform.

Please provide feedback

Please support the ScholarWorks@UMBC repository by emailing scholarworks-group@umbc.edu and telling us what having access to this work means to you and why it's important to you. Thank you.



Heliocentric Distance and Solar Activity Dependence of Sustained Quasi-radial Interplanetary Magnetic Field Occurrence

Brandon L. Burkholder^{1,2} , Li-Jen Chen² , Norberto Romanelli^{2,3} , Dave Sibeck², Jaye Verniero², Gina A. DiBraccio², Daniel Gershman² , and Menelaos Sarantos²

¹ University of Maryland Baltimore County, Baltimore, MD, USA

² NASA Goddard Space Flight Center, Greenbelt, MD, USA

³ University of Maryland College Park, College Park, MD, USA

Received 2023 February 10; revised 2023 June 12; accepted 2023 June 28; published 2023 August 7

Abstract

Planets close to their stars experience an interplanetary magnetic field (IMF) that is dominantly quasi-radial. Our solar system serves as a laboratory to study how the occurrence of quasi-radial IMF varies away from the star and under different stellar activities. Furthermore, on time and spatial scales relevant to magnetospheric physics, solar wind variability prevails in the form of structures generated both at the Sun and locally in the interplanetary space. The stationary Parker spiral model only approximates the large-scale structure of the IMF. Deviations from the Parker spiral often result in strongly radial magnetic fields that give rise to kinetic foreshock turbulence, which in turn can impact planetary magnetospheres. The relative significance of this type of interaction can be estimated statistically based on the occurrence rate of cases where the IMF is directed along the radial direction, leading to the entire day-side magnetosphere being downstream of the ion foreshock. We use observations covering radial distances from 0.1 to 10 au and more than 2 solar cycles to quantify the prevalence of radial IMFs throughout the heliosphere. Near Earth’s orbit, it is found that the occurrence rates of quasi-radial and southward IMF orientations are similar, and that the Pearson correlation coefficient is $\mathcal{R}_{xy} \sim -0.7$ calculated between quasi-radial IMF occurrence rate and solar activity. A negative correlation is demonstrated for radial distances extending to at least Mars but not to Saturn.

Unified Astronomy Thesaurus concepts: [Interplanetary magnetic fields \(824\)](#); [Planetary bow shocks \(1246\)](#); [Solar cycle \(1487\)](#)

1. Introduction

The interplanetary magnetic field (IMF) extends from the top of the solar corona to the edge of the heliosphere. The classical picture of this field is the Parker spiral (Parker 1958), and later the “ballerina skirt” (Rosenberg & Coleman 1969; Levy 1976). Parker (1958) derived the radial (B_r) and azimuthal (B_ϕ) components of the IMF with respect to radial distance from the Sun (r):

$$B_r \sim 1/r^2, B_\phi \sim 1/r.$$

Superposed on this background field are disturbances generated at the Sun and in situ in the solar wind (see Viall et al. 2021 and references therein), which are responsible for deflections of the magnetic field from the nominal Parker spiral direction. For a Parker spiral, the IMF direction at any radial distance is constant: it is the time variability introduced by the disturbances, which complicate the solar wind–magnetosphere coupling problem.

Long duration events of a few hours, with IMF $|B_r/B| > 0.9$, occur about 10% of the time at Earth (Watari et al. 2005; Pi et al. 2014). Orlove et al. (2013) interpreted these intervals as evidence for an interchange instability operating between two sources of different solar wind speed at low-latitudes on the Sun. In the Voyager 2 data, it was found that radial IMF events are rare in the outer heliosphere (Wang et al. 2003). From 1977 to 1982 between

radial distances of 1 and 10 au, they were detected on only $\sim 1.8\%$ of days. Those events that were observed were associated with gradually declining or steady solar wind flow speed, and only a small portion of the events were related to coronal mass ejections (CMEs). Wang & Sheeley (2015) later found the variation of the radial IMF strength is out of phase with that of the total CME occurrence rate (OR), with the latter closely following the sunspot number (SSN), but the IMF strength tending to peak just after sunspot maximum.

At Earth, IMF B_z (vertical component in geocentric solar magnetospheric coordinates) has been traditionally considered as the key factor in the solar wind–magnetosphere coupling (Russell 2000). This is because the planetary dipole presents a northward (positive B_z) magnetic field at the day-side. When the IMF B_z is directed southward (negative B_z), the IMF and Earth’s magnetic field are antiparallel, leading to erosion of the day-side magnetic flux via large-scale reconnection, and, if the driving is sustained, the Dungey cycle of global circulation (Dungey 1961). The cycle of substorm growth and recovery is also associated with southward IMF and the occurrence of day-side reconnection during southward IMF. Recently, Chen et al. (2021a), Ng et al. (2021) used global hybrid simulations with quasi-radial (QR) IMF to show that foreshock turbulence advecting into the downstream region of the quasi-parallel bow shock can create Earth-sized regions of southward IMF in the magnetosheath and initiate magnetopause reconnection where there would have otherwise been no magnetic shear between the IMF and Earth’s magnetic field.

All planets in our solar system have a bow shock, because the Alfvén transition region lies around $20 R_{\text{Sun}}$ (Kasper et al. 2021), and Mercury’s orbit is always $r > 60 R_{\text{Sun}}$. Therefore,



Original content from this work may be used under the terms of the [Creative Commons Attribution 4.0 licence](#). Any further distribution of this work must maintain attribution to the author(s) and the title of the work, journal citation and DOI.

Table 1
Near-Earth Magnetic Field Observations Used in This Study

Spacecraft Name	Date Range (yyyy/mm/dd)	Radii (au)	Data Volume (days)	Coordinates	Resolution (s)
ACE	1998/01/01–2022/01/03	0.97–1.01	8760	GSM	16
Wind	2004/06/01–2022/03/12	0.97–1.01	6443	GSM	60
ARTEMIS P1/P2	2011/01/01–2022/03/18	0.98–1.02	1449	GSM	3
MMS1	2017/01/01–2021/12/31	0.98–1.02	310	GSM	1/8 or 1/16

Notes. ARTEMIS and MMS radii correspond to Earth’s perihelion and aphelion. The data column displays the total amount of solar wind observations available during the date range. Geocentric solar magnetospheric (GSM).

the quasi-parallel bow shock processes that produce large magnetic disturbances (Kan et al. 1991) can be expected to occur at all the planets in our solar system when the IMF is strongly radial. In terms of comparative magnetospheres, the magnetic reconnection associated with radial IMF could mean bow shock processes are equal to or more important than the B_z component, depending on the planet under study. At Mercury, for example, the bow shock would be expected to be entirely quasi-parallel for the greatest portion of time due to the dominant B_r at small r . In addition, a recent study compared solitary magnetic structures associated with quasi-parallel shock geometry at Earth and Mars (Chen et al. 2022), concluding that the planet-sized foreshock turbulence can have space weather effects on the small (a few Mars radii in size) induced magnetosphere of Mars, while the effects on the relatively large terrestrial magnetosphere may only be short-lived reconnection and Earth-sized indents.

In the first part of this study, the observations from multiple near-Earth spacecraft are utilized to compare the prevalence of steady QR IMF intervals against steady southward IMF intervals. QR IMF is defined using the cone angle (see Section 2), while southward IMF is defined using the magnitude of the B_z component (in geocentric solar magnetospheric coordinates). These are different measures because the quasi-parallel bow shock geometry depends on the angle between the IMF and the shock normal, while the strength of antiparallel day-side magnetopause reconnection depends on the magnitude of the IMF B_z component. Note also that it is possible that the two magnetospheric coupling mechanisms can act simultaneously. However, the results show that while the different scenarios do occur at a similar rate they almost never occur at the same time. Then, the QR IMF OR is quantified including heliospheric coverage from closer to the Sun than Mercury’s orbit, out to the orbit of Saturn. This study aims to determine the likelihood of sustained QR IMF intervals at different radial distances from the Sun, on timescales motivated by terrestrial convection timescales relevant to space weather. Although these timescales may not be applicable to the other planets for the same reason, they are sufficient for capturing most major changes of the IMF direction, so for uniformity of the analysis, equal window sizes are used for all radial distances.

2. Data and Methods

The data for this study come from 10 spacecraft as outlined in Tables 1 and 2. Table 1 is for the near-Earth spacecraft. In Table 2, radial distances range from <0.1 au at perihelia of Parker Solar Probe (PSP) to ~ 9.5 au at the orbit of Saturn. The longest continuous observation comes from Advanced Composition Explorer (ACE), which covers 2 complete solar cycles.

Some of the spacecraft orbit the Sun (PSP; Mercury Surface, Space Environment, Geochemistry, and Ranging, hereafter MESSENGER, cruise; Wind; ACE; Juno cruise; Cassini cruise), so they are either always or mostly in the solar wind, and the other spacecraft orbit some target body (MESSENGER Mercury, Acceleration, Reconnection, Turbulence and Electrodynamics of the Moon’s Interaction with the Sun, hereafter ARTEMIS, Magnetospheric Multiscale; hereafter MMS; Mars Atmosphere and Volatile Evolution; hereafter MAVEN; and Cassini Saturn), requiring a sorting to get the solar wind observations only. The methods for sorting each different data set are described below.

PSP (Fox et al. 2016) offers a unique perspective from closer to the Sun than any other mission. The minimum radial distance achieved in this data set is 0.08 au. The FIELDS investigation (Bale et al. 2016) provides the vector magnetic field. The days before, during, and after each Venus flyby are not included in the data set (see Guo et al. 2021 for flyby dates).

MESSENGER (Santo et al. 2001; Solomon et al. 2001) carried a magnetometer (MAG) instrument (Anderson et al. 2007) between radial distances of Earth and Mercury, encountering Mercury and Venus multiple times during cruise before Mercury orbital insertion in 2011 March. During the cruise phase, the days before, during, and after each of the encounters are not included in our data set. In addition, there is heater contamination up to 2007 June, so this is where the data set begins (Boardsen et al. 2015). During the orbital phase, the bow shock standoff distance is taken as 0.2 Mercury radii larger than the most expanded case calculated by Winslow et al. (2013). The solar wind data is sorted based on the three-dimensional position of the spacecraft with respect to this nominal bow shock.

ACE (Stone et al. 1998) arrived at the Lagrange 1 (L1) point in 1997 December carrying a magnetometer (Smith et al. 1998). As part of the Global Geospace Science Program, the Wind spacecraft (Acuña et al. 1995) arrived at L1 later, in 2004 May, with a magnetometer (Lepping et al. 1995). Two entire solar cycles have elapsed since the arrival of ACE, and more than 1.5 solar cycles have elapsed since Wind arrived at L1, providing the opportunity to compare with solar activity.

Having originally been part of the Time History of Events and Macroscale Interactions during Substorms (THEMIS; Sibeck & Angelopoulos 2008) constellation, two spacecraft were moved to lunar orbit in 2011, forming ARTEMIS. These satellites spend a significant amount of time in the solar wind when not enveloped in the lunar wake or terrestrial magnetotail. For this study, the magnetic field data (Auster et al. 2008) from both spacecraft (ARTEMIS P1 and P2) are binned together. To avoid the lunar wake and magnetotail, it is

Table 2
Other Magnetic Field Observations Used in This Study

Spacecraft Name	Date Range (yyyy/mm/dd)	Radii (au)	Data Volume (days)	Coordinates	Resolution (s)
Parker Solar Probe	2018/10/02–2021/09/30	0.08–0.94	733	RTN	60
MESSENGER cruise	2007/08/01–2011/02/28	0.3–0.7	1005	RTN	1
MESSENGER Mercury	2011/04/01–2015/04/30	0.31–0.47	359	MSO	60
Juno Cruise	2011/08/25–2016/06/29	1.0–5.4	1442	SE	60
MAVEN	2014/10/10–2021/05/14	1.4–1.7	145	SS	1
Cassini cruise	2001/01/01–2004/06/20	5.0–9.0	1077	RTN	60
Cassini Saturn (1)	2004/07/01–2012/06/02	9.0–10.1	425	RTN	1
Cassini Saturn (2)	2004/07/01–2016/12/31	9.0–10.1	230	KSM	60

Notes. Satellites orbiting a planet are labeled with radii corresponding to the perihelion and aphelion. The data column displays the total amount of solar wind observations available during the date range. Radial, tangential, normal (RTN). Mercury solar orbital (MSO). Sun equator (SE). Sun-state (SS). Kronocentric solar magnetospheric (KSM).

required that the spacecraft x -coordinate >0 in both geocentric solar ecliptic and selenocentric solar ecliptic coordinates. The solar wind data amount from Table 1 shows the total for both spacecraft (1449 days) from more than 11 yr of observations. These data are 17% of the total mission for one spacecraft.

MMS (Burch et al. 2016) is a four spacecraft constellation whose separations are tens to hundreds of kilometers, small enough that a single spacecraft is sufficient for this statistical study. The data from the fluxgate magnetometer instrument (Torbert et al. 2016) on board MMS1 is sorted into solar wind and nonsolar wind by comparing the x -component of the spacecraft location to the x -component of the bow shock nose (Burkholder & Otto 2019; Burkholder et al. 2020) as reported by NASA OMNIWeb (Papitashvili & King 2020). Column (4) from Table 1 shows the total amount of data taken by MMS in the solar wind using this criteria is about 20% of the total mission. The start date from column (4) in Table 1 is 2017 January 1 even though the mission began in 2015 because there is almost no solar wind data until 2017.

Data are available during the Juno (Bolton et al. 2017) cruise phase from the MAG instrument (Connerney et al. 2017) covering radial distances between Earth and Jupiter. The encounter with Earth in 2013 October is not included in our data set. Once Juno arrived at Jupiter, with the exception of a few bow shock crossings (Hospodarsky et al. 2017), it has spent a majority of the time inside the magnetosphere, so none of the orbital data is included in this study.

MAVEN (Jakosky et al. 2015) orbits Mars with an apogee of less than 2 Mars radii. Since the typical bow shock standoff distance is similar to this (Gruesbeck et al. 2018), its MAG instrument (Connerney et al. 2015) can observe the IMF for some portion of the orbit. Sorting of the data according to solar wind and nonsolar wind is outlined in Halekas et al. (2017).

Magnetometer observations from two phases of the Cassini (Russell 2003) mission are utilized. The cruise phase covers interplanetary space between Jupiter and Saturn. Cassini then entered a Saturn orbital phase until the grand finale in 2017. In Table 1, there are 2 rows that represent the orbital phase. The row Cassini Saturn (1) ends in 2012 because the plasma instrument ceased to operate, such that relevant plasma boundaries could no longer be unambiguously identified (Delamere et al. 2013, 2015). During the data range in the Cassini Saturn (1) row, knowing the location of every boundary crossing allows to maximize the number of solar wind observations. The row Cassini Saturn (2) is different

because it extends all the way through the end of 2016. This data set is sorted using an overly restrictive requirement that the spacecraft be outside 50 Saturn radii. The reason for the inclusion of both data sets is to cover the greatest portion of a solar cycle and to compare the results where the two data sets overlap.

To analyze all the above data sets together, the observations with higher resolution than 1 minute were time-averaged to 1 minute (see time resolutions for each spacecraft in Tables 1 and 2). The degree to which the IMF points in the radial direction can be quantified by the cone angle, which is defined

$$\phi = \frac{180}{\pi} \arccos \frac{|B_r|}{|B|} \in [0, 90].$$

Note, the r -direction is defined by the instantaneous Sun–planet vector for a few of the data sets (GSM, MSO, KSM), and it is defined by the instantaneous Sun–spacecraft vector for the others (see coordinate systems in column (5), Tables 1 and 2). Given the small size of the satellite orbits around the planet compared to those planets’ orbits about the Sun, these two different definitions of the r -direction are taken as equivalent. This assumption allows to compare the QR IMF OR from the different spacecraft without any coordinate transformations, since only the radial component and the magnetic field strength are needed to calculate ϕ . We refer to $\phi < 20^\circ$ as QR, although the results in this study are insensitive to changes of 5° – 10° from this threshold. Such QR cone angles have been identified as preferential for the development of foreshock turbulence upstream of the day-side magnetopause (Russell et al. 1983; Chen et al. 2021b).

The OR is a quantity used in this study defined as the ratio of the total number of IMF observations with a QR ϕ versus the total number of IMF observations by that spacecraft. Accordingly, the QR OR would be 1 if in the data set the IMF was always QR, and 0 if it was never QR. In addition, since the intent is to quantify the occurrence of solar wind intervals with a steady QR IMF, the duration OR (DOR) is defined similar to OR but takes a ratio using a sliding window ϕ rather than the individual data points (slide length is half window length). The window sizes of 10, 20, and 30 minutes are chosen based on convection and substorm timescales at Earth (Jayachandran & MacDougall 2007). For uniformity of the analysis, we also choose the same window sizes for all radial distances, even though the timescales are not physically justifiable in terms of convection timescales for other planets. Windowing of the data leads to the question of how to assign a single value of ϕ to

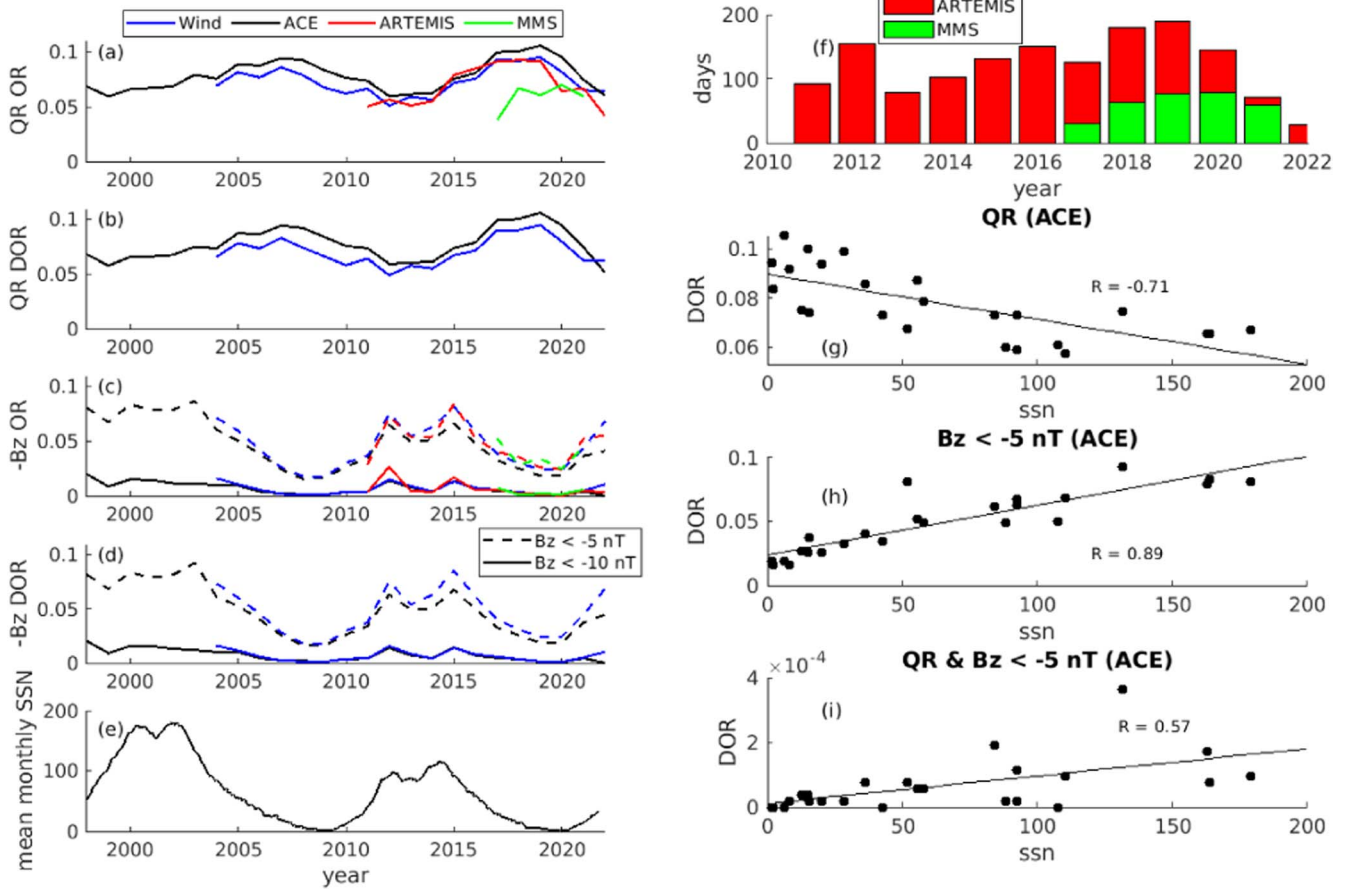


Figure 1. (a) Occurrence rate (OR) of quasi-radial (QR) IMF as a function of year for Wind (blue), ACE (black), ARTEMIS (red), and MMS (green). (b) Duration occurrence rate (DOR), using the mode of the observations in each 20 minutes window) of sustained QR IMF as a function of year. (c) OR of southward IMF as a function of year with $B_z < -5$ nT in dashed lines and $B_z < -10$ nT in solid lines. (d) DOR of southward IMF. (e) Monthly mean sunspot number (SSN). (f) Coverage histograms for ARTEMIS (red) and MMS (green). (g) Scatter plot of 20 minutes window QR DOR vs. SSN for ACE. (h) Scatter plot of southward ($B_z < -5$ nT) DOR vs. SSN for ACE. (i) Scatter plot of DOR for windows satisfying both QR and southward IMF ($B_z < -5$ nT) criteria. All scatter plots cover years 1998–2022. Spacecraft colors are the same in (a)–(d).

each window. The results in this study were obtained using both the mean (average of ϕ in each window) and mode (most likely ϕ in each window), and the conclusions were insensitive to these different operations. Note also that for the planetary orbiters we have made no attempt to remove foreshock contamination present in the solar wind data. With sufficient statistics, and depending on how far each specific spacecraft ventures into the solar wind, it is only a small portion of the data affected by foreshock contamination. Fortunately, since the data set has extensive coverage, the results can be compared from the planetary orbiters with spacecraft orbiting the Sun, which have no foreshock contamination. It is found that at similar radial distances the spacecraft orbiting the Sun can confirm the results of the planetary orbiters, with differences that can be accounted for by the solar cycle variation.

3. Results.

3.1. Near-Earth Comparison of QR versus Southward IMF

Figure 1 shows the summary of near-Earth IMF observations from Wind, ACE, ARTEMIS, and MMS (see Table 1). Figures 1(a)–(d) show the QR OR, QR DOR, southward OR, and southward DOR, respectively. The (20 minutes window length) DOR is only calculated for Wind and ACE because they have continuous solar wind coverage for the windowing

process. The OR and DOR are plotted at a yearly cadence, and the different colors correspond to the different spacecraft (blue, Wind; black, ACE; red, ARTEMIS; green, MMS). In Figures 1(c) and (d), the solid lines represent southward IMF with $B_z < -10$ nT, and the dashed lines are southward IMF with $B_z < -5$ nT. A comparison of the Wind and ACE results shows that OR and DOR are equivalent measures, which was expected because the data sets are large. Averaged over all years, the amount of time that the QR IMF interaction occurs at Earth ($\sim 7\%$) is similar to the amount of time that the southward IMF ($B_z < -5$ nT) interaction occurs ($\sim 5\%$), with greater year-to-year variability in the southward IMF. The only discrepancy between the different spacecraft is the QR OR observed by MMS. Though, the southward OR observed by MMS agrees with the other spacecraft, which suggests that the deficit of QR IMF observed by MMS is due to the foreshock contamination (since the QR IMF is difficult to observe when the spacecraft is immersed in foreshock fluctuations).

Figure 1(e) shows monthly mean SSN (retrieved from the NOAA Space weather prediction center),⁴ as a measure of solar activity level. The QR IMF observed by all the near-Earth spacecraft shows an anticorrelation with the solar cycle. ACE and Wind have continuous solar wind coverage, but for MMS

⁴ <https://www.swpc.noaa.gov/>

and ARTEMIS, it is important that sufficient solar wind statistics exist for every year to confirm the solar cycle dependence for these spacecraft. Figure 1(f) shows the coverage histogram for MMS (green) and ARTEMIS (red). ARTEMIS has close to 100 days of solar wind coverage for all years except 2022, leaving no doubt as to the validity of the statistics. MMS has only 30 days of solar wind data in 2017, which is significantly less than the following years, and the QR OR observed by MMS during that year was remarkably low. Though, it is the case that the southward OR observed by MMS in 2017 agrees with ACE, Wind, and ARTEMIS, meaning the deficit observed by MMS in 2017 is likely not due to lack of statistics.

In Figure 1(g), a Pearson correlation coefficient of $\mathcal{R}_{xy} = -0.71$ is demonstrated for the ACE data. The black line is a linear fit to the scattered points, on axes that are SSN versus QR DOR. The anticorrelation of QR DOR and solar activity has been found for longer duration windows of a few hours (Watari et al. 2005; Pi et al. 2014). Figure 1(h) is the scatter plot of SSN versus southward DOR ($B_z < -5$ nT) for ACE data. As opposed to the anticorrelation observed for the QR IMF, the southward IMF shows a positive correlation with solar cycle, and Pearson coefficient of $\mathcal{R}_{xy} = 0.89$. Since the solar activity level is correlated with IMF strength (Larrodera & Cid 2020), this demonstrates that the stronger IMF B_z component is more likely to be observed during solar maximum, varying along with total magnetic field strength, while the QR IMF is observed more often when the magnetic field strength is weaker.

The statistical analysis in Figure 1 leads to the conclusion that the terrestrial magnetosphere will more likely be exposed to sustained QR IMF at solar minimum compared to solar maximum, with a variation of $\sim 3\%$ of the time. A significant component of negative IMF B_z occurs more often at solar maximum, and, for $B_z < -5$ nT, varies by $\sim 5\%$ from solar minimum to maximum. IMF with $B_z < -10$ nT occurs only $\sim 1\%$ – 2% of the time but also has a positive correlation with solar activity level. Figure 1(i) demonstrates that most of the time these different IMF conditions are not met simultaneously. Each point is the DOR of 20 minutes IMF windows satisfying both the QR ($\theta < 20^\circ$) and southward ($B_z < -5$ nT) criteria. These events make up about 1 in every 5000 windows, which for 20 minutes windows corresponds to ~ 5 windows yr^{-1} . For comparison, the QR windows occur with a frequency of about 1 in every 15 windows, or about 2000 windows yr^{-1} .

3.2. QR IMF throughout the Heliosphere

Examples of 2 hr time series at different radial distances from the Sun are shown in Figure 2 from (a)–(b) PSP, (c)–(d) MESSENGER cruise, (e)–(f) Juno cruise, and (g)–(h) Cassini cruise, in Sun–spacecraft radial-tangential-normal (RTN) coordinates. The left panel for each spacecraft shows full resolution magnetic field observations (these are the highest available resolutions, 1 minute averages are used for the statistical analysis), and the right panel shows the same time series smoothed with a 20 minutes window (black left-side axis). The smoothed observations are shown to demonstrate the effect of the 20 minutes windowing that is performed on the data to calculate DOR. Each interval of observations shows QR IMF for an extended duration (see ϕ in orange right-side axis Figures 2(b), (d), (f), (h)).

For the Parker Spiral IMF model, the magnetic field lines take on the shape of an Archimedean spiral. In this simplified picture, the only free parameter is the solar wind speed v_{sw} . For $v_{\text{sw}} = 400 \text{ km s}^{-1}$, $\phi = 24^\circ$ at Mercury, $\phi = 47^\circ$ at Earth, $\phi = 58^\circ$ at Mars, $\phi = 80^\circ$ at Jupiter, and $\phi = 84^\circ$ at Saturn. Based on this model, the Juno and Cassini observations of QR IMF are particularly surprising. However, the Parker spiral model only represents the background direction of the IMF. The QR IMF events like those in Figure 2 are perturbations to the background magnetic field orientation. Note also that near the Sun perturbations are producing less QR IMF, while at Jupiter and Saturn (and even the Earth) large perturbations are the main mechanism to produce QR IMF.

Figure 3(a) shows the OR of QR IMF observations as a function of r . For those spacecraft in interplanetary space, the observations are binned with bin widths of 0.1 au at $r < 1$ au, and bin widths of 1 au for $r > 1$ au. The QR OR observed by the satellites orbiting a planet is plotted at r corresponding to the average orbital distance of the planet. At Mercury this could be responsible for a slight aliasing due to the large orbital eccentricity, but would be insignificant for the other planets in this study. Note that PSP goes below 0.1 au in this data set, but the points are plotted at bin center. Similarly, there is not actually a gap between Earth and Juno observations since the first Juno bin covers radial distances from 1 to 2 au. The Cassini Saturn (1) and (2) results were combined for this figure, and the same for all near-Earth spacecraft. The error bars are calculated by considering each month of data in each distance bin, and taking the standard deviation of the monthly ORs. The dependence on r is well fit by the power law given in dashed red, with variations due to the solar cycle dependence. The heliocentric distance power law can be expected for the occurrence of transient solar wind phenomena. For instance, directional discontinuities are observed with a heliocentric distance power law (Söding et al. 2001). Furthermore, transient events on the Sun, such as solar flares, occur at a rate that follows a power law dependent on the intensity of the event (Verbeek et al. 2019).

Figure 3(b) shows the DOR of QR IMF as a function of radial distance for 10 (red), 20 (green), and 30 (blue) minute window lengths. These different window lengths do not have a huge effect on the DOR, but it is expected that for much longer windows the rates will drop significantly. The DORs are only calculated for the spacecraft that are always in the solar wind, so the windowing process is uninterrupted. ACE and Wind results were averaged. Similar to Figure 1, the OR and DOR agree almost exactly (compare Figures 3(a) and (b)), reflecting the fact that there are good statistics for all radial distances covered. Ultimately, the difference between OR and DOR is the latter captures short fluctuations that are smoothed over during the windowing. Closer to the Sun DOR is higher than OR, because, when the fluctuations are smoothed out, the background magnetic field is QR, while farther from the Sun the windowing does not have much of an effect, due to the background field not being QR.

Based on Figure 3, the IMF is QR $\sim 10\%$ – 15% of the time at the orbit of Mercury, $\sim 5\%$ – 10% at Earth, $\sim 2\%$ – 3% at Jupiter, and $< 1\%$ at Saturn. At the orbit of Mars, Figure 3(a) shows that the Juno cruise data predicts a QR IMF $\sim 5\%$ of the time, while MAVEN orbiting Mars indicates 3% – 4% , which can be accounted for by the solar cycle variation (see Figure 4).

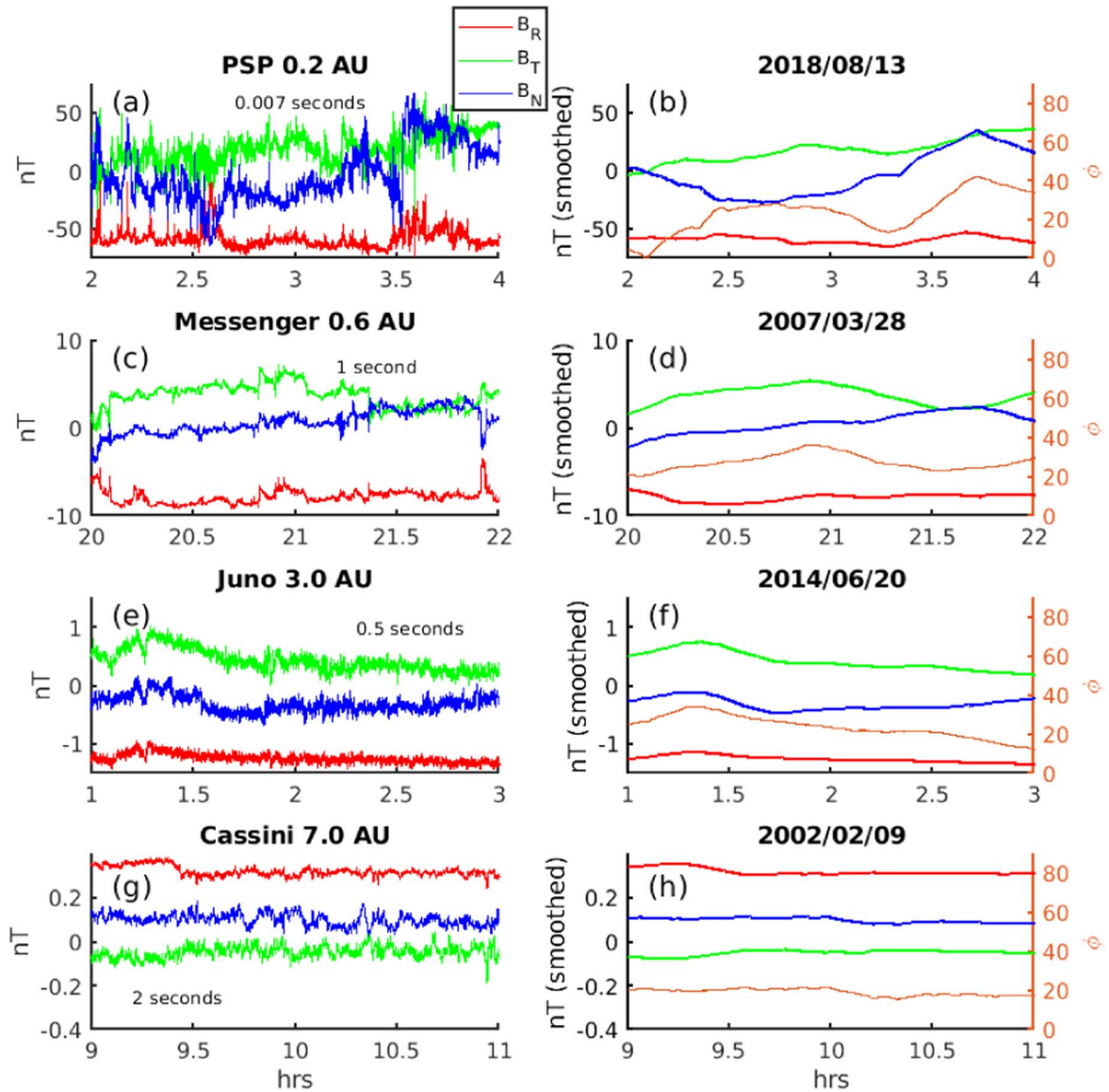


Figure 2. Example 2 hr time series from (a)–(b) PSP, (c)–(d) MESSENGER cruise, (e)–(f) Juno, and (g)–(h) Cassini cruise. (a), (c), (e), (g) are the radial-tangential-normal (RTN) magnetic field vector observed at full resolution, with heliocentric distance in the title and measurement cadence written in black text. (b), (d), (f), (h) are the same time series smoothed using a 20 minutes window (left-side, black axis), with date in the title, and the IMF clock angle $\phi = \arccos\left[\frac{B_T}{|B|}\right]$ on the right-side orange axis.

These results depend on the choice of $\phi = 20^\circ$ as a critical angle, but the general trends of the data are insensitive to small changes in the angle. This result for Earth is larger than that previously reported in a study that searched for longer durations of 6 hr and greater (Watari et al. 2005), but in agreement with a study searching for durations of 4 hr and greater (Pi et al. 2014). Our results also are in agreement with Voyager observations (Wang et al. 2003) and a recent study of Saturn’s bow shock (Sulaiman et al. 2016).

Figure 4(a) shows the OR of QR IMF as a function of year for all spacecraft in this study, which remain at the same radial distance from the Sun (with only ACE at the near-Earth radial distance). The coverage plots are also given in Figures 4(c)–(d) in the same format as Figure 1(f), for reference. Figure 4(b) shows the monthly SSN again to compare with the QR OR at different planets. Alongside ACE (black), the anticorrelation of solar activity with QR OR is apparent for MESSENGER

Mercury (magenta) and MAVEN (green), but not Cassini (cyan). This suggests the anticorrelation of solar activity with QR OR holds at least as close to the Sun as Mercury and at least as far away as Mars. Beyond the orbit of Mars at ~ 1.5 au, the next long-term observation at a single radial distance is Cassini (black) at Saturn (9.5 au). The reason for the inclusion of the two different orbital data sets is to show that they agree for the years 2004–2012, justifying the use of the Cassini Saturn (2) data set (with overly restrictive sorting requirements) to compare with a greater portion of the solar cycle. The Cassini Saturn (2) data set does not have a point for every year because the available solar wind observations are clustered. At Saturn, the QR ORs are a few percent or less, and compared against more than half of a solar cycle, there is variation but no correlation. Based on these results, the anticorrelation of QR OR with solar activity ceases to hold at a distance between 1.5 and 9.5 au.

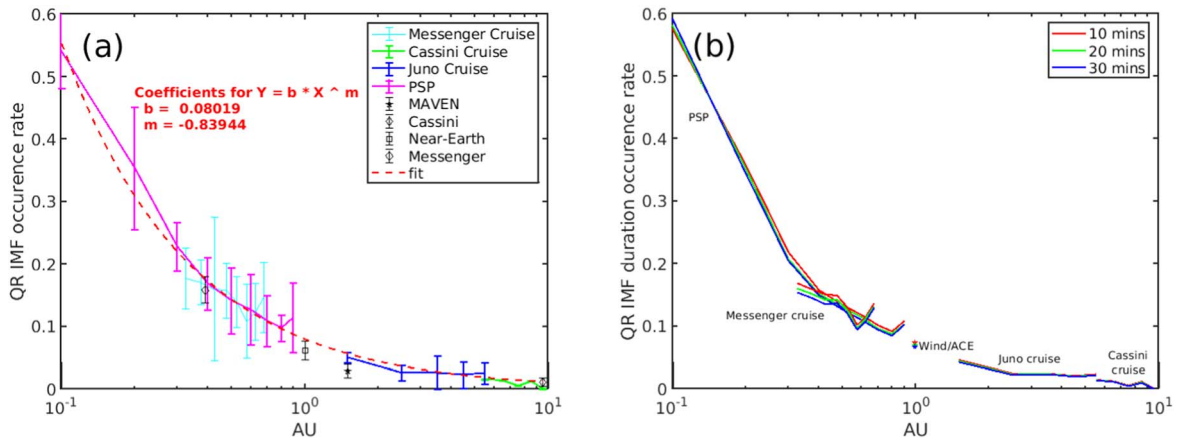


Figure 3. (a) Occurrence rate of quasi-radial (QR) IMF as a function of radial distance from the Sun. The dashed red line is a heliocentric distance power-law fit with parameters given in red text. The error bars represent a monthly standard deviation (described in main text). THEMIS, Wind, ACE, and MMS1 results are averaged. (b) Duration occurrence rate of sustained QR IMF using the mode of each window and only including the spacecraft that remain in the solar wind (ACE and Wind results are averaged). Red, green, and blue traces correspond to 10, 20, and 30 minutes window lengths.

4. Discussion and Conclusions

The steady-state Parker spiral model of the heliospheric magnetic field predicts that the IMF should never be QR outside the orbit of Mercury. Any given time series of magnetometer observations from spacecraft in the solar wind will demonstrate this is not the case, and there is a particular difficulty to consider in that the solar wind contains structures with a wide range of scale sizes. For instance, magnetic field switchbacks (de Wit et al. 2020) closer to the Sun are regions where the radial magnetic field component reverses, occurring about 8% of the time in Ulysses observations at high-latitude (Balogh et al. 1999). Other than the “quiescent” regions (Short et al. 2022) containing no switchbacks, they are ubiquitous near the Sun (Bale et al. 2019; Kasper et al. 2019), appearing in dense, irregular clusters (Bale et al. 2021). The switchbacks near the Sun can be associated with non-QR IMF in those regions where the background field (which is generally QR) has been bent into the switchback shape (see, for instance, Fedorov et al. 2021 Figure 4 showing non-QR IMF for ~ 5 minutes between intervals of reversed polarity). This ultimately means that the switchbacks are leading to a lower observed QR OR close to the Sun. Further away from the Sun it is an open question whether the switchbacks are as numerous as near the Sun (Fedorov et al. 2021), and switchback-like structures have been observed at radial distances as far as 2.9 au (Yamauchi et al. 2002). At Earth and beyond, the background Parker spiral field is not radially dominated, implying that switchback-like structures would be a source for the QR IMF.

Regardless of the source of the QR IMF, observations in this paper show QR IMF occurring all the way to the orbit of Saturn, where the Parker spiral angle is essentially 90° . To put the QR IMF solar cycle dependence into perspective with other known properties of the solar cycle variation, the largest radial IMF strengths are observed just after solar maximum (Wang & Sheeley 2015), and the largest number of CMEs are observed at solar maximum (Cremades & Bothmer 2004). Our results add to this list that QR cone angles occur most often at solar minimum.

Based on our analysis, the anticorrelation of solar activity with QR occurrence in the inner heliosphere means the large-scale solar wind structures (Viall et al. 2021) generated at the Sun (namely CMEs and stream interaction regions) are more

likely leading to less QR IMF. This can be concluded because these structures are more often present in the solar wind when the solar activity level is higher, and this is during the time when the least QR IMF intervals are observed, at radial distances from the orbit of Mercury to at least Mars. In the outer heliosphere, no solar cycle correlation is found at Saturn. It can be speculated that this is because of either or both of the following effects: (1) the solar wind at Saturn is significantly eroded, having expanded so far into the heliosphere that there is little structure remaining, (2) having a Parker spiral angle close to 90° requires a very significant perturbation to get to QR IMF conditions, which are not able to survive out to 10 au if they are generated at the Sun, so these are perturbations generated in situ in the solar wind, and it is possible these do not have any or some different dependence on solar activity. In future work, we will consider other available data sets (Voyagers, Pioneer, Ulysses) to better understand the transition.

Of course, QR is not the only IMF orientation that produces a quasi-parallel bow shock geometry that can influence the magnetosphere (Fairfield 1969; Vuorinen et al. 2019; Ma et al. 2020). In fact, since quasi-parallel is defined as everywhere that $\theta_{Bn} < 45^\circ$, with θ_{Bn} the angle between the bow shock normal and IMF; along the full extent of the shock surface, this condition is satisfied for about half of the surface area during any given IMF orientation. However, the motivation for this study is the circumstance in which the bow shock is entirely quasi-parallel upstream of the subsolar magnetopause, leading to the day-side magnetosphere being enveloped in fluctuations generated in the foreshock. It has been found that foreshock disturbances are strongest for QR IMF (Troitskaya et al. 1971; Greenstadt & Olson 1976; Wolfe et al. 1980; Russell et al. 1983) and therefore of the greatest immediate interest to space weather prediction beyond the traditional day-side reconnection scenario.

Lastly, it should be noted that, at Earth, the IMF B_z component may be the most geoeffective parameter, but this is not the case throughout the solar system. In particular, when the magnetosphere is not much larger than the planet, like Mars, the foreshock turbulence can be associated with significant space weather effects (Chen et al. 2021a). For planets other than Earth, a full understanding of the relative effectiveness of different magnetospheric driving mechanisms, such as large-scale reconnection (Dungey 1961) and viscous

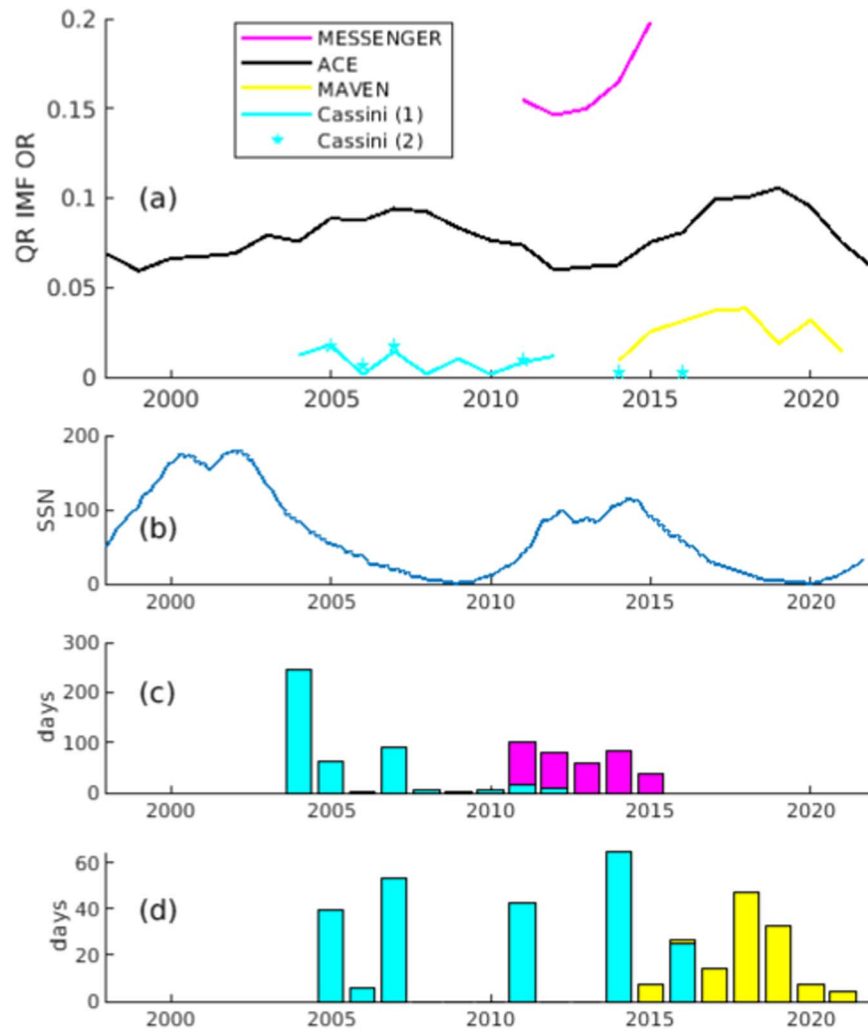


Figure 4. (a) Occurrence rate (OR) of quasi-radial (QR) IMF as a function of year at different planets in the solar system. Colors correspond to magenta, MESSENGER at Mercury; black, ACE at Earth; yellow, MAVEN at Mars; cyan, Cassini at Saturn. Cassini Saturn (1) is represented by the solid cyan line, and Cassini Saturn (2) is represented by the cyan stars (see Table 2). (b) Monthly mean sunspot number (SSN). (c)–(d) Data coverage for each spacecraft in the same format as Figure 1(f). (c) Shows Cassini Saturn (1) and MESSENGER Mercury while (d) shows Cassini Saturn (2) and MAVEN.

interactions (Axford 1964), has not been fully determined. Masters (2018) supported the possibility of a predominantly viscous-like interaction between the solar wind and the giant planet magnetospheres, but admitted that an understanding of energy flow through a planetary magnetosphere requires a combination of understanding the overall external solar wind driving with consideration of internal drivers. Therefore, in an effort to help build an understanding of the overall solar wind driving at all the planets, this study has quantified the prevalence of sustained QR IMF as a function of heliospheric distance. Our results provide a baseline to estimate how often each planet’s bow shock will have a quasi-parallel geometry upstream of a large section of the day-side magnetopause, leading to potential space weather effects.

5. Software and Third Party Data Repository Citations

All of the data for this study are available from either the NASA Space Physics Data Facility <https://cdaweb.gsfc.nasa.gov/> or the NASA Planetary Data System <https://pds.nasa.gov/>.

Acknowledgments

We acknowledge use of NASA/GSFC’s Space Physics Data Facility’s OMNIWeb. Funding for this work is provided by the NASA MMS mission. N.R. is supported by NASA under Award 80GSFC21M0002.

ORCID iDs

Brandon L. Burkholder <https://orcid.org/0000-0001-8702-5806>
 Li-Jen Chen <https://orcid.org/0000-0002-4768-189X>
 Norberto Romanelli <https://orcid.org/0000-0001-9210-0284>
 Daniel Gershman <https://orcid.org/0000-0003-1304-4769>
 Menelaos Sarantos <https://orcid.org/0000-0003-0728-2971>

References

- Acuña, M., Ogilvie, K., Baker, D., et al. 1995, *SSRv*, 71, 5
- Anderson, B. J., Acuña, M. H., Lohr, D. A., et al. 2007, *SSRv*, 131, 417
- Auster, H., Glassmeier, K., Magnes, W., et al. 2008, *SSRv*, 141, 235
- Axford, W. 1964, *P&SS*, 12, 45
- Bale, S. D., Badman, S. T., Bonnell, J. W., et al. 2019, *Natur*, 576, 237
- Bale, S. D., Goetz, K., Harvey, P. R., et al. 2016, *SSRv*, 204, 49

- Bale, S. D., Horbury, T. S., Velli, M., et al. 2021, *ApJ*, **923**, 174
- Balogh, A., Forsyth, R. J., Lucek, E. A., Horbury, T. S., & Smith, E. J. 1999, *GeoRL*, **26**, 631
- Boardsen, S. A., Jian, L. K., Raines, J. L., et al. 2015, *JGRA*, **120**, 10207
- Bolton, S. J., Lunine, J., Stevenson, D., et al. 2017, *SSRv*, **213**, 5
- Burch, J. L., Moore, T. E., Torbert, R. B., & Giles, B. L. 2016, *SSRv*, **199**, 5
- Burkholder, B. L., Nykyri, K., & Ma, X. 2020, *JGRA*, **125**, e2020JA027978
- Burkholder, B. L., & Otto, A. 2019, *JGRA*, **124**, 8227
- Chen, L.-J., Halekas, J., Wang, S., et al. 2022, *GeoRL*, **49**, e2021GL097600
- Chen, L.-J., Ng, J., Omelchenko, Y., & Wang, S. 2021a, *GeoRL*, **48**, e2021GL093029
- Chen, L.-J., Wang, S., Ng, J., et al. 2021b, *GeoRL*, **48**, e2020GL090800
- Connerney, J. E. P., Benn, M., Bjarno, J. B., et al. 2017, *SSRv*, **213**, 39
- Connerney, J. E. P., Espley, J., Lawton, P., et al. 2015, *SSRv*, **195**, 257
- Cremades, H., & Bothmer, V. 2004, *A&A*, **422**, 307
- de Wit, T. D., Krasnoselskikh, V. V., Bale, S. D., et al. 2020, *ApJS*, **246**, 39
- Delamere, P. A., Otto, A., Ma, X., Bagenal, F., & Wilson, R. J. 2015, *JGRA*, **120**, 4229
- Delamere, P. A., Wilson, R. J., Eriksson, S., & Bagenal, F. 2013, *JGRA*, **118**, 393
- Dungey, J. W. 1961, *PhRvL*, **6**, 47
- Fairfield, D. H. 1969, *JGR*, **74**, 3541
- Fedorov, A., Louarn, P., Owen, C. J., et al. 2021, *A&A*, **656**, A40
- Fox, N. J., Velli, M. C., Bale, S. D., et al. 2016, *SSRv*, **204**, 7
- Greenstadt, E. W., & Olson, J. V. 1976, *JGR*, **81**, 5911
- Gruesbeck, J., Espley, J., Connerney, J., et al. 2018, *JGRA*, **123**, 4542
- Guo, Y., Thompson, P., Wirzburger, J., et al. 2021, *AcAau*, **179**, 425
- Halekas, J. S., Ruhunusiri, S., Harada, Y., et al. 2017, *JGRA*, **122**, 547
- Hospodarsky, G. B., Kurth, W. S., Bolton, S. J., et al. 2017, *GeoRL*, **44**, 4506
- Jakosky, B. M., Lin, R. P., Grebowsky, J. M., et al. 2015, *SSRv*, **195**, 3
- Jayachandran, P. T., & MacDougall, J. W. 2007, *EP&S*, **59**, e29
- Kan, J. R., Mandt, M. E., & Lyu, L. H. 1991, *SSRv*, **57**, 201
- Kasper, J. C., Bale, S. D., Belcher, J. W., et al. 2019, *Natur*, **576**, 228
- Kasper, J. C., Klein, K. G., Lichko, E., et al. 2021, *PhRvL*, **127**, 255101
- Larrodera, C., & Cid, C. 2020, *A&A*, **635**, A44
- Lepping, R. P., Acuña, M. H., Burlaga, L. F., et al. 1995, *SSRv*, **71**, 207
- Levy, E. 1976, *Natur*, **261**, 394
- Ma, X., Nykyri, K., Dimmock, A., & Chu, C. 2020, *JGRA*, **125**, e2020JA028209
- Masters, A. 2018, *GeoRL*, **45**, 7320
- Ng, J., Chen, L.-J., & Omelchenko, Y. A. 2021, *PhPl*, **28**, 092902
- Orlove, S. T., Smith, C. W., Vasquez, B. J., et al. 2013, *ApJ*, **774**, 15
- Papitashvili, N. E., & King, J. H. 2020, OMNI 5-min Data, NASA Space Physics Data Facility, doi:10.48322/gbpg-5r77
- Parker, E. N. 1958, *ApJ*, **128**, 664
- Pi, G., Shue, J.-H., Chao, J.-K., et al. 2014, *JGRA*, **119**, 7005
- Rosenberg, R. L., & Coleman, P. J., Jr. 1969, *JGR*, **74**, 5611
- Russell, C. 2000, *ITPS*, **28**, 1818
- Russell, C. T. 2003, The Cassini-Huygens Mission. Overview, Objectives and Huygens Instrumentarium, Vol. 104 (Berlin: Springer)
- Russell, C. T., Luhmann, J. G., Odera, T. J., & Stuart, W. F. 1983, *GeoRL*, **10**, 663
- Santo, A., Gold, R., McNutt, R., et al. 2001, *P&SS*, **49**, 1481
- Short, B., Malaspina, D. M., Halekas, J., et al. 2022, *ApJ*, **940**, 45
- Sibeck, D. G., & Angelopoulos, V. 2008, *SSRv*, **141**, 35
- Smith, C., L'Heureux, J., Ness, N., et al. 1998, *SSRv*, **86**, 613
- Söding, A., Neubauer, F. M., Tsurutani, B. T., Ness, N. F., & Lepping, R. P. 2001, *AnGeo*, **19**, 667
- Solomon, S., McNutt, R., Gold, R., et al. 2001, *P&SS*, **49**, 1445
- Stone, E., Frandsen, A., Mewaldt, R., et al. 1998, *SSRv*, **86**, 1
- Sulaiman, A. H., Masters, A., & Dougherty, M. K. 2016, *JGRA*, **121**, 4425
- Torbert, R. B., Russell, C. T., Magnes, W., et al. 2016, *SSRv*, **199**, 105
- Troitskaya, V. A., Plyasova-Bakunina, T. A., & Gul'Elmi, A. V. 1971, *DoSSR*, **197**, 1312
- Verbeeck, C., Kraaikamp, E., Ryan, D. F., & Podladchikova, O. 2019, *ApJ*, **884**, 50
- Viall, N. M., DeForest, C. E., & Kepko, L. 2021, *FrASS*, **8**, 139
- Vuorinen, L., Hietala, H., & Plaschke, F. 2019, *AnGeo*, **37**, 689
- Wang, C., Richardson, J. D., Burlaga, L. F., & Ness, N. F. 2003, *JGRA*, **108**, 1205
- Wang, Y.-M., & Sheeley, N. R. J. 2015, *ApJL*, **809**, L24
- Watari, S., Vandas, M., & Watanabe, T. 2005, *JGRA*, **110**, A12102
- Winslow, R. M., Anderson, B. J., Johnson, C. L., et al. 2013, *JGRA*, **118**, 2213
- Wolfe, A., Lanzerotti, L., & MacLennan, C. 1980, *JGRA*, **85**, 114
- Yamauchi, Y., Suess, S. T., & Sakurai, T. 2002, *GeoRL*, **29**, 21